### Title

On the Structure and Stability of BaAl4-Type Ordered Derivatives in the Sr–Au–Sn System for the 600 °C Section




### Journal

Zeitschrift für anorganische und allgemeine Chemie, 641(2)

### ISSN

0044-2313



### Authors

Lin, Qisheng
Zhang, Yuemei
Taufour, Valentin
et al.



### Publication Date

2015-02-01

### DOI

10.1002/zaac.201400549

Peer reviewed

Journal of Inorganic and General Chemistry
ZAAC
Zeitschrift für anorganische und allgemeine Chemie
www.zaac.wiley-vch.de
ARTICLE

DOI: 10.1002/zaac.201400549

# On the Structure and Stability of $BaAl_4$-Type Ordered Derivatives in the Sr–Au–Sn System for the 600 °C Section

**Qisheng Lin,[a] Yuemei Zhang,[b] Valentin Taufour,[a,c] Tej Nath Lamichhane,[a,c] Sergey L. Bud'ko,[a,c] Paul C. Canfield,[a,c] Kevin Dennis,[a] and Gordon Miller*[a,b]**

*Dedicated to Professor Hans-Jörg Deiseroth on the Occasion of His 70th Birthday*

**Keywords:** Solid-state structures; Electronic structure; X-ray diffraction; $BaAl_4$-type; Intermetallic phases

**Abstract**. The well-known $BaAl_4$-type structure consists of three ordered ternary derivatives, i.e., $BaNiSn_3$- (*I*4*mm*), $ThCr_2Si_2$- (*I*4/*mmm*), and $CaBe_2Ge_2$-type (*P*4/*nmm*). Few systems, such as Ba-Au-Sn, have been confirmed to manifest all three types as a function of valence electron count. In this work, the $SrAu_xSn_{4-x}$ solid solution at the 600 °C section was studied thoroughly using both single crystal and powder X-ray diffraction. The crystal structures and phase width for the $CaBe_2Ge_2$-type $SrAu_xSn_{4-x}$ solid solution were established to be $a$ = 4.6528(2)–4.6233(3) Å and $c$ = 11.3753(4)–11.2945(10) Å for $x \approx$ 1.65(1)–2.19(1). In the structure of $SrAu_2Sn_2$, no Au/Sn mixing was found, but for $x < 2$ compositions, Au/Sn mixings were only located at the Wyckoff 2*a* (¾ ¼ 0) site and for $x > 2$ compositions, at the 2*b* (¾ ¼ ½) site. Differential scanning calorimetry (DSC) analyses indicated that no phase transition occurred for the $CaBe_2Ge_2$-type $SrAu_xSn_{4-x}$ phase up to 950 °C. Attempts to synthesize the $ThCr_2Si_2$- and $BaNiSn_3$-type $SrAu_xSn_{4-x}$ phases under the same reaction conditions were unsuccessful, and the $BaNiSn_3$-type phase could not be attained even at a pressure of 3 GPa. The instability of a $BaNiSn_3$-type "$SrAuSn_3$" was investigated by both DSC measurements and first principles electronic structure calculations.

## Introduction

The tetragonal $BaAl_4$ (*I*4/*mmm*) structure is one of the most frequently adopted structural types for intermetallic compounds.[1] This structure features square pyramidal layers built with basal square nets of Al that are alternatively capped by apical Al atoms above and below. Ordered ternary derivatives (excluding superstructures with multiple base unit cells) of $BaAl_4$-type phases can be grouped into three general sub-families depending on how the square nets and apical sites are colored: (1) the centric $ThCr_2Si_2$ (*I*4/*mmm*, the ternary version of $BaAl_4$); (2) the noncentrosymmetric $BaNiSn_3$ (*I*4*mm*); and (3) the centric $CaBe_2Ge_2$ (*P*4/*nmm*) types.[1b] The square pyramidal layers in all these three structural types are similar in topology to that of the iron arsenide layers in superconducting $LaO_{1-x}F_xFeAs$.[2] For this reason, $BaAl_4$-type ternary derivatives are attracting renewed attention in the fields of condensed matter physics and materials chemistry.[3] Consequently, more and more precious metal-based $BaAl_4$-type ternary derivatives, e.g., $BaPtSi_3$,[4] $SrPd_2As_2$,[5] $SrPd_2Ge_2$,[6] $SrPt_2As_2$,[7] and $LaPd_2Sb_2$,[8] have been found to exhibit superconductivity at low temperatures. These results encouraged our synthetic exploration of Au-based $BaAl_4$-type derivatives.[9] After all, superconducting binary compounds of Au with II–III A or II–III B group elements are already reported.[10] Moreover, the compound $SrAuSi_3$ has been synthesized using high pressure means, and it is the first Au-based superconductor with noncentrosymmetric symmetry.[11]

Gold-containing ternary phases adopting the $BaNiSn_3$-, $ThCr_2Si_2$-, or $CaBe_2Ge_2$-type structures have been reported for many *A*-Au-*T* systems (*A* = alkaline earth and rare earth metals, *T* = triels and tetrels).[1b,12] Because gold and triel (group 13) or tetrel (group 14) elements may exhibit mixed occupancies on various crystallographic sites, it is important to establish the composition range of each $BaAl_4$-type derivative so that accurate structural information can be obtained and no pertinent phase is overlooked. Recently, examination of the Ba-Au-Sn system[9] revealed all three types $BaAu_xSn_{4-x}$ depending on $x$: $BaNiSn_3$- for $x$ = 0.78(1)–1, $ThCr_2Si_2$- for $x$ = 1.38(1)–1.47(1), and $CaBe_2Ge_2$-type for $x$ = 1.52(1)–2.17(1). Occurrence of all three structure types as a function of composition and, thus, valence electron count in the same system had been unprecedented, so these results are far-reaching. As noted,[9] distinct differences between the two distinct "122" types should be readily apparent in light of their different lattice

* Prof. Dr. G. Miller
Fax: +1-515-294-0105
E-Mail: gmiller@iastate.edu
[a] Division of Materials Science & Engineering
Ames Laboratory, US-DOE
Ames, Iowa, 50011, U.S.A
[b] Department of Chemistry
Iowa State University
Ames, Iowa, 50011, U.S.A
[c] Department of Physics and Astronomy
Iowa State University
Ames, Iowa, 50011, U.S.A
Supporting information for this article is available on the WWW under **http://dx.doi.org/10.1002/zaac.201400549** or from the author.

Dedicated Cluster

 

types on the condition that the low-intensity peaks allowed by the P-lattice have not been misinterpreted as arising from any impurity phases. However, the difference between the acentric "113" phase and the centric $ThCr_2Si_2$-type "122" phase is elusive because *I*4*mm* and *I*4/*mmm* have exactly the *same* systematic absence conditions.

Continuation of this effort shifted our attention to the Sr-Au-Sn system. A survey of the literature revealed that the $CaBe_2Ge_2$-type $SrAu_2Sn_2$ phase probably was first synthesized in 1974.[13] However, no synthetic information and crystallographic data about this phase were available in databases. As to the acentric $BaNiSn_3$-type phase, no pertinent information can be found in the literature. Recently, *Tkachuk* and *Mar*[14] reported the single crystal structure of the $ThCr_2Si_2$-type $SrAu_{1.4(1)}Sn_{2.6(1)}$, in which Au/Sn mixtures were found at both basal and apical sites. The homogeneity range of this phase established from powder X-ray diffraction data was $1.3 \leq x \leq 2.2$ at the 700 °C section. They also concluded that the hypothetical $CaBe_2Ge_2$-type "$SrAu_2Sn_2$" phase had smaller (270 meV/f.u.) total energy than the corresponding $ThCr_2Si_2$-type structure.

Therefore, this work continued with the following goals: (1) to seek the $BaNiSn_3$-type phase under both ambient and high pressure conditions; (2) to determine the single crystal structure of the $CaBe_2Ge_2$-type phase; and (3) to establish phase widths of and phase gaps among the $CaBe_2Ge_2$-, $ThCr_2Si_2$-, and possibly $BaNiSn_3$-type (if it exists) $SrAu_xSn_{4-x}$ phases of the 600 °C section, the same temperature examined for $BaAu_xSn_{4-x}$.[9] At the time the writing of this article was nearly completed, we noticed that the $CaBe_2Ge_2$-type $SrAu_xSn_{4-x}$ ($1.7 \leq x \leq 2.2$) structures had just been reported by *Pöttgen* and co-workers.[15] According to their report, complete ordering between Au and Sn was observed in $SrAu_2Sn_2$ crystals that had been annealed at 377 °C, whereas various Au/Sn mixed occupancies at Wyckoff 2*a*, 2*b*, or 2*c* sites were found for other compositions, probably resulting by the lower annealing temperature.

Our systematic studies of the 600 °C section yielded interesting outcomes including subtle changes in crystal structures. Herein, we report that (1) only the $CaBe_2Ge_2$-type $SrAu_xSn_{4-x}$, $x = 1.65(1)$–$2.19(1)$, were found at the 600 °C section, in contrast to the Ba-Au-Sn system, which contains all three $BaAl_4$-type ordered derivative phases;[9] (2) Au/Sn mixtures were only observed in basal planes of $SrAu_xSn_{4-x}$ ($x \neq 2$) structures, in contrast to those of *Pöttgen* and co-workers;[15] (3) differential scanning calorimetry (DSC) shows that no phase transition occurs from the $CaBe_2Ge_2$-type to the $ThCr_2Si_2$-type phase up to 950 °C, suggesting that the $ThCr_2Si_2$-type phases reported before[14] might have been misinterpreted; (4) the $BaNiSn_3$-type "$SrAuSn_3$" could not be obtained at either ambient or high pressure (ca. 3 GPa) reaction conditions, as also supported by DSC data; and (5) the instability of "$SrAuSn_3$" could be theoretically explained with the help of first principles electronic structure calculations.

## Results and Discussion

### *Phase Width of the $CaBe_2Ge_2$-type $SrAu_xSn_{4-x}$*

Figure 1 shows XRD powder patterns for products of six selected $SrAu_ySn_{4-y}$ reactions with $y = 1.25$–$2.50$. The powder pattern of the $y = 1.75$ and 2.00 reaction can be completely indexed by a unit cell with *P*4/*nmm* symmetry, $a \approx 4.66$ Å, $c \approx 11.30$ Å, suggesting single phase products of the $CaBe_2Ge_2$-type structure. In contrast, the products of $y = 1.25$–$1.50$ reactions, which were loaded below the reported lower limit of the homogeneity range, consist of various percentages of $SrAuSn_2$ phase.[16] The refined compositions of crystals from $y = 1.40$ reaction is within $3\sigma$ difference from that of $y = 1.25$ reaction, $SrAu_{1.68(1)}Sn_{2.32(1)}$ versus $SrAu_{1.65(1)}Sn_{2.35(1)}$. Therefore, these values shall be very close to the lower limit of the homogeneity range of the $CaBe_2Ge_2$-type $SrAu_xSn_{4-x}$ according to the lever rule.

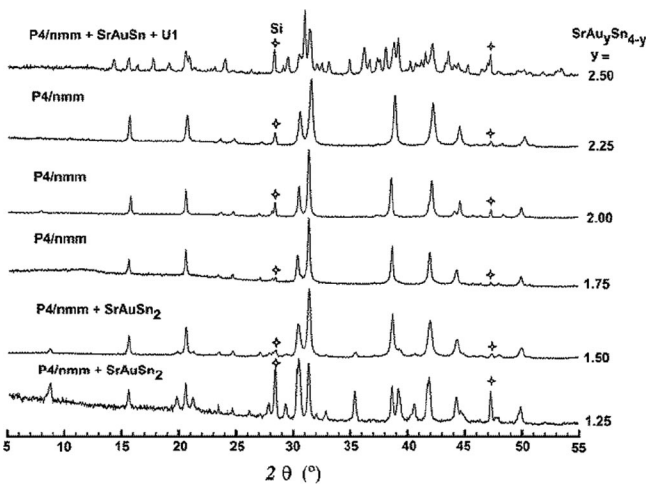


**Figure 1.** XRD powder patterns of $SrAu_ySn_{4-y}$ reactions with $y = 1.25$–$2.5$. Major products of each reaction are marked (*P*4/*nmm* denotes the title $CaBe_2Ge_2$-type phase, and U1 denotes an unidentified phase). Grey stars denote peaks of Si standard.

On the other end, the XRD pattern for the $y = 2.25$ reaction also appears as a single phase product of the $CaBe_2Ge_2$-type $SrAu_xSn_{4-x}$. However, the composition refined from single crystal data for this product is $SrAu_{2.19(1)}Sn_{1.81(1)}$. The small difference ($6\sigma$) between the refined and initial compositions suggests that a trace of impurity (not detected by powder XRD) should exist in the product, which in turn means that the refined composition should be very close to the upper limit of the phase boundary of the $CaBe_2Ge_2$-type $SrAu_xSn_{4-x}$ solid solution. Subsequently, it is not surprising that the XRD powder pattern of the reaction for $y = 2.50$ shows a mixture of SrAuSn,[17] the $CaBe_2Ge_2$-type phase, and an as yet unknown phase. However, no $BaNiSn_3$- and $ThCr_2Si_2$-type phases were found in the whole composition range we studied. It turns out that the homogeneity range of $SrAu_xSn_{4-x}$, $x = 1.65(1)$–$2.19(1)$, established for the 600 °C section is close to that for the 377 °C section, $x = 1.76$–$2.22$.[15] In comparison, the homogeneity range of the $CaBe_2Ge_2$-type $BaAu_xSn_{4-x}$ phase is also similar, $1.52(1) \leq x \leq 2.17(1)$.[9]

### *Structure and Coloring of the $CaBe_2Ge_2$-type $SrAu_xSn_{4-x}$*

Because the relationships among the $CaBe_2Ge_2$-, $BaNiSn_3$-, and $ThCr_2Si_2$-type structures have been frequently discussed

Dedicated Cluster

before,[1,9] we simply emphasize the subtle structural changes of the $CaBe_2Ge_2$-type $SrAu_xSn_{4-x}$ at different compositions.

Figure 2 shows unit cells of the two end members of the $SrAu_xSn_{4-x}$ solid solution and the intermediate $SrAu_2Sn_2$ without Au/Sn mixtures. While the apical atoms capping respective squares (dashed lines) do not change for all compositions, the major differences among these three compositions lie in decorations of the basal square planes, which are generated by the Wyckoff 2*a* or 2*b* positions. For $SrAu_2Sn_2$, the top square is defined by Au at Wyckoff 2*a* site and bottom square by Sn at the 2*b* site. For Sn-rich compositions ($x < 2$), e.g., $SrAu_{1.65(1)}Sn_{2.35(1)}$ in Figure 2(a), excess Sn (compared to $SrAu_2Sn_2$) only mixes with Au at the Wyckoff 2*a* site (forming the top square) but not with Au at the apical positions. In contrast, for Au-rich compositions ($x > 2$), e.g., $SrAu_{2.19(1)}Sn_{1.81}$ in Figure 2(c), excessive Au only mixes with Sn at the Wyckoff 2*b* site (forming the bottom square) but not with Sn at the apical positions. A similar Au/Sn ordering phenomenon has been observed in the $CaBe_2Ge_2$-type $BaAu_xSn_{4-x}$ phases.[18] In general, the structures of $SrAu_xSn_{4-x}$ by *Pöttgen* and coworkers are also consistent with ours, except that they refined additional Au/Sn mixings (within 3 standard deviations) at the Au apical site in $SrAu_{2.16}Sn_{1.84}$ (A) and $SrAu_{2.22}Sn_{1.78}$, and at both basal planes as well as the Au apical site in $SrAu_{2.16}Sn_{1.84}$ (B).[15] It is possible that the different annealing temperature influences the Au/Sn chemical ordering in $SrAu_xSn_{4-x}$, particularly for Au-rich compositions.

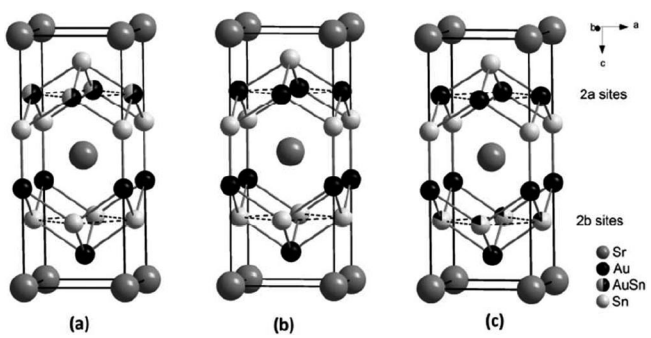


**Figure 2.** Unit cells of (a) $SrAu_{1.65(1)}Sn_{2.35(1)}$, (b) $SrAu_2Sn_2$, and (c) $SrAu_{2.19(1)}Sn_{1.81(1)}$ with the $CaBe_2Ge_2$-type structure (*P4/nmm*). For straightforward comparison with other $BaAl_4$-type derivative structures, origin of each unit cell is shifted to the Sr (¼ ¼ *z*) sites. Dashed black lines denote basal square nets.

The choice of how a structure is decorated by different atoms is called the "coloring problem",[19] and the observed result is influenced by optimizing the sum of the site and bond energy terms of the total electronic energy. Let's first look at the "site energy" term, which can be evaluated by valence electron populations for related sites in $SrAu_2Sn_2$ by Bader charge analyses from VASP calculations. For example, to examine where excessive Sn will locate in $SrAu_xSn_{4-x}$ ($x < 2$) structures, only a comparison of valence electron populations on the two independent Au sites will be required, whereas to examine where excessive Au will be populated in $x > 2$ compositions, a comparison of the two Sn sites is necessary. As given in Table 1, Au2 at the Wyckoff 2*a* site has smaller valence electron population than Au1 at the 2*c* site, suggesting that the less electronegative Sn atom prefers to occupy the 2*a* site (or the basal $Au_4$ square) in Sn-rich $SrAu_xSn_{4-x}$ phases. Similarly, the Sn3 (2*b*) site has a slightly larger valence electron population than the Sn4 (2*c*) site, a signature of site preference for the more electronegative Au atom in Au-rich $SrAu_xSn_{4-x}$ phases. The results are consistent with our experimental observations. As to the "bond energy" term, apparently, it can be assessed by a comparison of the sum of integrated COHP (ICOHP) values for different atomic arrangements. In the case of Sn-rich compositions ($x < 2$), two hypothetical $SrAu_{1.5}Sn_{2.5}$ models were built with excess Sn either located at (I) the basal $Au_4$ squares or (II) at the apical Au sites (cf. Figure S1, Supporting information) As for the Au-rich compositions ($x > 2$), two hypothetical $SrAu_{2.5}Sn_{1.5}$ models were built with excess Au located (III) at the basal $Sn_4$ squares and (IV) at the apical Sn sites. As a result, the sum of ICOHP values for model I is about 168 meV/f.u. higher than that of II (Table S1, Supporting Information), indicating that excess Sn mixed with the apical Au site is favorable for $x < 2$ compositions in terms of the bond energy. It appears that the site and bond energy terms are competing in the Sn-rich compositions, but, overall, the influence of the site energy term is larger than the bond energy term (see below for a comparison of total energies). As to models III and IV, the sum of ICOHP values for model III is 665 meV/f.u. lower than that of IV. Therefore, both site and bond energy terms suggest excess Au in $x > 2$ compositions would prefer to replace Sn atoms at the basal sites rather than the apical sites, consistent with experimental results. In fact, the VASP total energy for model I is lower than that for II by 163.03 meV/f.u., whereas the total energy for model III is 203.53 meV/f.u. lower in energy than that for IV.

### *Thermal Analysis of the $CaBe_2Ge_2$-type $SrAu_xSn_{4-x}$*

Since the $CaBe_2Ge_2$-type $SrAu_xSn_{4-x}$ [$x$ = 1.65(1)–2.19(1)] phases were attainable at 600 °C (this work) or below,[15] whereas the $ThCr_2Si_2$-type phases ($x$ = 1.3–2.2) were obtained after annealing treatments at 700 °C,[14] at first we speculated that these two phases could be low- and high-temperature polymorphs. After all, temperature-dependent structural transitions between the $ThCr_2Si_2$- and $CaBe_2Ge_2$-type structures have been reported for many systems such as $REIr_2Si_2$ (*RE* = Y, La, Nd, Gd, Dy, Ho),[20] in which the $ThCr_2Si_2$-type was

**Table 1.** Electron population of $SrAu_2Sn_2$ evaluated by Bader charge analysis.

| $SrAu_2Sn_2$ | Sr(2*c*) (4s, 4p, 5s) | Au1(2*c*) (5d, 6s) | Au2(2*a*) (5d, 6s) | Sn3(2*b*) (5s, 5p) | Sn4(2*c*) (5s, 5p) |
|---|---|---|---|---|---|
| Electron population | 8.63 | 12.22 | 11.80 | 3.70 | 3.66 |
| Net charge | +1.37 | –1.22 | –0.80 | +0.30 | +0.34 |

Dedicated Cluster

found as low-temperature and the $CaBe_2Ge_2$-type as high-temperature polymorphs. In a different region of the Sr-Au-Sn system, two temperature-dependent polymorphs were also found for $Sr_3Au_8Sn_3$: a $La_3Al_{11}$-type structure (space group *Immm*) at 550 °C and higher temperatures; and a $Ca_3Au_8Ge_3$-type structure (*Pnnm*) at 400 °C.[21] In addition, first principles calculations on $SrAu_2Sn_2$ indicated that the $CaBe_2Ge_2$-type structure had lower total energy by 270 meV/f.u. than the $ThCr_2Si_2$-type.[14]

The $CaBe_2Ge_2$-type pure phase product of "$SrAu_{1.75}Sn_{2.25}$" (cf. Figure 1) was used for DSC measurements to search for a possible phase transition between the $CaBe_2Ge_2$- and $ThCr_2Si_2$-type structures above 600 °C. As illustrated in Figure 3, the heating/cooling curves only show the melting point of "$SrAu_{1.75}Sn_{2.25}$" (X-ray pure phase product) at around 818 °C on heating and the freezing point at 808 °C; no other endo- or exothermic peaks representing any phase transition could be observed between room temperature and ca. 950 °C. (Note the small peak at around 770 °C in the heating curve could be caused by an unexpected disturbance, as evidenced by its zigzag shape and the absence of a corresponding effect in the cooling curve.) XRD powder patterns shown in the inset also indicate that no phase (structural) change occurs pre- and post-DSC scans. Therefore, annealing treatments at 600 °C and 700 °C should yield the same phase. In fact, an independent synthesis of $SrAu_2Sn_2$ by arc melting followed by annealing at 700 °C for 10 d yielded the $CaBe_2Ge_2$-type phase, too. The work of *Pöttgen* and co-workers[15] also did not find the $ThCr_2Si_2$-type phase at 377 °C.

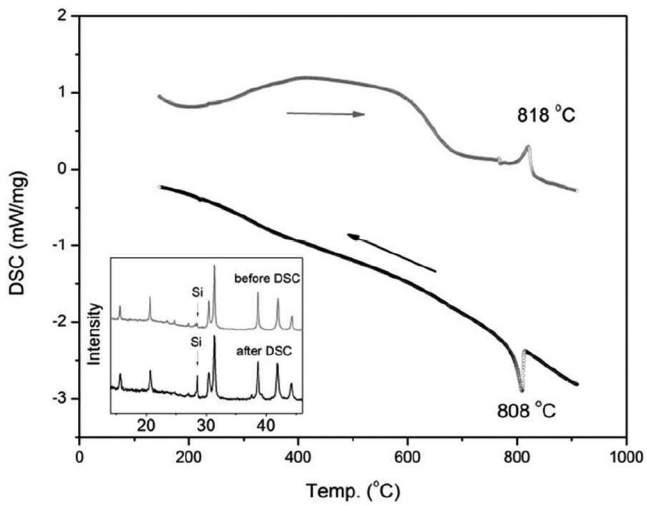


**Figure 3.** DSC data for products of nominal "$SrAu_{1.75}Sn_{2.25}$" on heating (gray) and cooling (black). Inset shows enlarged XRD powder patterns before (at room temperature) and after DSC scans.

### *Thermal Analysis of "$SrAuSn_3$"*

Synthetic attempts at $SrAu_ySn_{4-y}$ with lower Au content ($y$ = 0.75–1.50) did not yield an acentric $BaNiSn_3$-type "$SrAuSn_3$," in contrast to the Ba-Au-Sn system.[9] Thus, to examine if "$SrAuSn_3$" is thermodynamically unstable (or the reaction "$SrAuSn_3$" → $SrAuSn_2$ + Sn occurs during solidification), the product of a nominal "$SrAuSn_3$" reaction, which contains a mixture of $SrAuSn_2$ and Sn in 1:1 proportion, was studied by DSC measurements. The DSC data, Figure 4, show the endothermic peaks for melting of Sn (242 °C) and $SrAuSn_2$ (ca. 753 °C) on heating, together with an endothermic peak at 647 °C arising from the dissolution of $SrAuSn_2$ into Sn liquid. This dissolution process accounts for the absence of a sharp peak for the melting of $SrAuSn_2$ on heating. In contrast, sharp exothermic peaks denoting the freezing points of Sn (225 °C) and $SrAuSn_2$ (725 °C) were observed on cooling. XRD powder patterns pre- and post-DSC measurements are essentially the same (inset), indicating no phase changes. It appears that the $BaNiSn_3$-type "$SrAuSn_3$" is a thermodynamically unstable phase. Theoretical analyses (below) also support this statement.

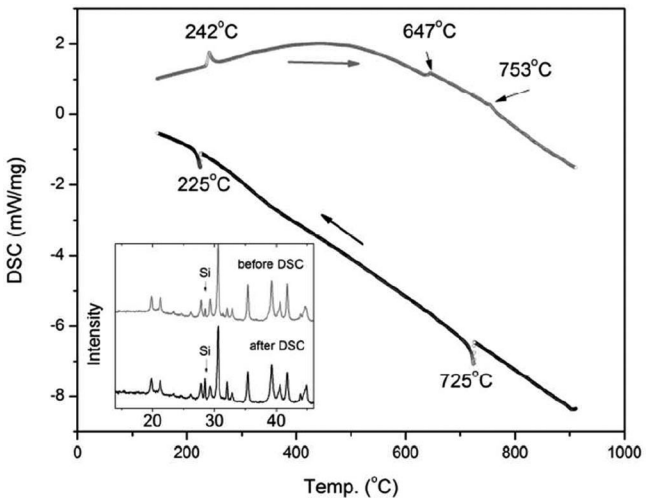


**Figure 4.** DSC data for products of the "$SrAuSn_3$" reaction on heating (gray) and cooling (black). Inset shows enlarged XRD powder patterns pre- and post-DSC scans.

### *The Instability of "$SrAuSn_3$"*

VASP calculations were employed to evaluate the total energies of "$SrAuSn_3$", together with that of Sn, $SrAuSn_2$,[16] $BaAuSn_2$,[22] and $BaAuSn_3$[9] for comparison. Geometry optimization was carried out using VASP non-spin polarized calculations for all structures. The total energy differences between $AAuSn_3$ and "$AAuSn_2$ + Sn" ($A$ = Sr, Ba) at 0 K gives the Gibbs free energy differences ($\Delta G$) for reactions "$AAuSn_2$ + Sn → $AAuSn_3$". As shown in Table 2, the calculated $\Delta G$ for

**Table 2.** Calculated VASP total energies (eV/f.u.) for Sn, $AAuSn_2$, $AAuSn_3$ ($A$ = Sr, Ba) and Gibbs free energy changes ($\Delta G$) for the reaction $AAuSn_2$ + Sn → "$AAuSn_3$" ($A$ = Sr, Ba) at 0 K.

| | $A$ = Ba (exp.) [a] | $A$ = Ba (opt.) [a] | $A$ = Sr (opt.) [a] |
|---|---|---|---|
| $E_{Sn}$ | –3.786 | –3.799 | –3.799 [b] |
| $E_{AAuSn2}$ | –15.283 | –15.336 | –14.861 |
| $E_{AAuSn3}$ | –19.188 | –19.294 | –18.592 |
| $\Delta G$ /eV | –0.119 | –0.159 | +0.069 |

a) Exp. stands for experimental structure, and opt. stands for optimized structure. b) Tetragonal Sn is used for VASP calculations.



 

the reaction of "$BaAuSn_2$ + Sn → $BaAuSn_3$" is always negative, no matter whether experimental or optimized structural data were used for the calculations. On the other hand, the reaction of "$SrAuSn_2$ + Sn → $SrAuSn_3$" has a positive $\Delta G$, which is energetically unfavorable.

To gain some insights about these total energy calculations, an examination of electronic band structures and analyses of COHPs for the interatomic orbital interactions in $BaAuSn_3$ and "$SrAuSn_3$" prove useful. As shown in Figure 5, the Fermi levels ($E_F$) of both $BaAuSn_3$ and "$SrAuSn_3$" fall on a doubly degenerate band at the Brillouin zone center (Γ). This band arises primarily from $p_x/p_y$ orbitals at the Au and Sn sites and shows interlayer Au–Sn π-antibonding (π*) overlap (cf. Figure 5c). The degeneracy and π* character of the band at $E_F$ is a typical signature of a possible electronic instability. The band structures differ, however, at $E_F$ for the P point, where a nondegenerate band from "$SrAuSn_3$" lies very close to $E_F$, but the same band for $BaAuSn_3$ is shifted 0.4 eV above $E_F$ (Figure 5b). This band involves a mixture of s and $z^2$ orbitals at the Ba/Sr sites with Au–Sn σ-antibonding (σ*) s-s orbitals (cf. Figure 5c). Thus, "$SrAuSn_3$" exhibits greater potential for an electronic instability than $BaAuSn_3$. In fact, both are formally 15-electron species, which are rather electron-rich for this family of structures.[12,13,23]

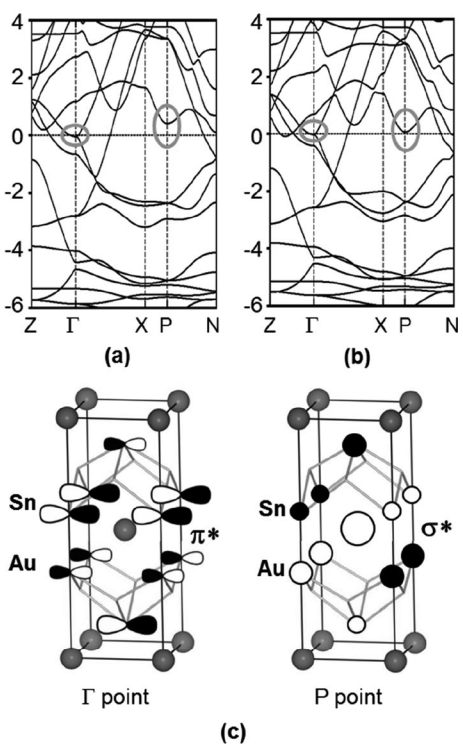


**Figure 5.** Non-spin polarized band structures of the body-centered tetragonal (a) $BaAuSn_3$ and (b) $SrAuSn_3$ along $Z$ (π/$a$, π/$a$, π/$c$)-$\Gamma$ (0, 0, 0)-$X$ (0, 0, π/$c$)-$P$ (π/2$a$, π/2$a$, π/2$c$)-$N$ (0, π/$a$, 0). Depictions of the π* and σ* crystal orbitals close to $E_F$ at the Γ and P points are included in (c).

A COHP analysis provides a broader perspective of chemical bonding features. Examination of the Au-Sn COHP curves, shown in Figure S2 (Supporting Information), reveal that the interlayer Au-Sn interactions in both $BaAuSn_3$ and "$SrAuSn_3$" are optimized at $E_F$. Therefore, the Au–Sn π* and σ* bands precisely at $E_F$ contribute to the occurrence of the bonding crossover. From the point of view of structural stability, an evaluation of integrated COHP (ICOHP) values, listed in Tables S4–S5 (Supporting Information), will provide more insights. The total ICOHP for "$SrAuSn_3$" is 0.012 eV/f.u. less negative than that of "$SrAuSn_2$ + Sn", whereas, for $BaAuSn_3$ it is 0.31 eV/f.u. more negative than the ICOHP value obtained from $BaAuSn_2$ + Sn, results that are consistent with the total energies in Table 2. The main differences in these total ICOHP values arise not from the $AAuSn_3$ structures, but with the $AAuSn_2$ structures. The matrix effect of the formal cations leads to smaller interatomic distances in the Sr compounds than in the Ba compounds. However, the relative changes in ICOHP values for $AAuSn_2$ ($A$ = Sr, Ba) reveal marked enhancements of Sr–Au and Sr–Sn interactions in $SrAuSn_2$ relative to the analogous Ba–Au and Ba–Sn interactions in $BaAuSn_2$ by 0.53 eV/f.u., whereas the total ICOHP values within the [$AuSn_2$] substructure differ by just 0.075 eV/f.u. Thus, the apparent thermodynamic instability of "$SrAuSn_3$" to date can be rationalized by both electronic instabilities in its electronic structure at $E_F$, as well as enhanced "Sr anion" bonding in $SrAuSn_2$.

## Conclusions

Switching the cation (A) from Ba to Sr in $BaAl_4$-type $AAu_xSn_{4-x}$ structures yields significant changes in their chemistry to produce only the $CaBe_2Ge_2$-type $SrAu_xSn_{4-x}$ phase at the 600 °C section. According to our single crystal analyses, Au/Sn mixings in the $CaBe_2Ge_2$-type $SrAu_xSn_{4-x}$ structures shift from the Wyckoff 2$a$ (¾ ¼ 0) site for $x < 2$ to the 2$b$ (¾ ¼ ½) site for $x > 2$ compositions, whereas no Au/Sn mixing occurs for $x = 2$, same as those seen in the $CaBe_2Ge_2$-type $BaAu_xSn_{4-x}$ phase. The absence of the acentric $BaNiSn_3$-type $SrAu_xSn_{4-x}$ phase has been examined by high pressure syntheses and DSC and theoretical analyses. This work also confirms that the $ThCr_2Si_2$-type $SrAu_xSn_{4-x}$ phase does not exist in the system.

## Experimental Section

**Synthesis:** The starting materials included as-received Au particles (99.999 %, BASF), dendritic Sr pieces (99.95 %, Alfa Aesar), with surfaces manually cleaned by a surgical blade, and Sn shot (99.99 %, Alfa Aesar). Mixtures of designed molar proportions (with total 400 mg) were loaded into Ta tubes (with one end weld-sealed) in an argon-filled glovebox ($H_2O$ < 0.1 ppm by volume). After the Ta tubes were completely weld-sealed they were enclosed in evacuated $SiO_2$ jackets ($P < 10^{-5}$ Torr). Reactions with nine different proportions "$SrAu_ySn_{4-y}$" ($y$ = 0.75, 1.00, 1.25, 1.40, 1.50, 1.75, 2.00, 2.25, 2.50) were run at 800 °C for 6 h, quenched in water, then annealed at 600 °C for 6–30 d. (Note: *To avoid confusion that could incur from differences between loaded and refined compositions*, $SrAu_ySn_{4-y}$ *is used to describe loaded proportions, whereas* $SrAu_xSn_{4-x}$ *for refined compositions*.) These proportions were designed according to the results obtained from the $BaAu_xSn_{4-x}$ system, in which the $BaNiSn_3$-,

Dedicated Cluster

$ThCr_2Si_2$-, and $CaBe_2Ge_2$-type phases were found within this range. However, except that the $y = 0.75$ and 1.00 reactions yielded mixtures of $SrAuSn_2$[16] and Sn, $CaBe_2Ge_2$-type phases were found among the products of all other reaction mixtures. All products have metallic luster, and are inert to air at room temperature for at least 12 months.

The $CaBe_2Ge_2$-type $SrAu_xSn_{4-x}$ phases were also obtained by heating nominal $SrAu_ySn_{4-y}$ ($y$ = 1.50–2.00) mixtures at 950 °C for 2 h, followed by slow cooling to 600 °C at a rate of 5 °K·h$^{-1}$, annealing there for one week, and then quenching into water. The reaction loaded as "$SrAuSn_3$" under this condition yielded the mixture of $SrAuSn_2$[16] and Sn. In addition, the $CaBe_2Ge_2$-type $SrAu_2Sn_2$ phase was also synthesized by arc melting reactions of stoichiometric $SrAu_2Sn_2$, followed by annealing at 700 °C for 10 d; whereas the nominal "$SrAuSn_3$" sample made under arc melting and annealing at 800 °C produced a mixture of $SrAuSn_2$[16] and Sn.

Since nominal "$SrAuSn_3$" reactions always produced a mixture of $SrAuSn_2$ and Sn under ambient pressure, we hypothesized that "$SrAuSn_3$" could be stabilized via high pressure, similar to its isovalent analogue $SrAuSi_3$.[11] The starting materials for high pressure syntheses were either mixtures of metals in "113" stoichiometry or "$SrAuSn_3$" that had been pre-reacted at 950 °C (i.e., a mixture of $SrAuSn_2$ and Sn). For all cases, starting materials were pelleted under a pressure of 4000 tons and loaded into BN crucibles that were held by a customarily designed cube that was placed in the center of an anvil cell.[24] The desired pressure was achieved by transferring the large uniaxial vertical force generated from a hydraulic ram to the anvil cell, to the cube, to the crucible, and then to the sample. For all high-pressure reactions, 3 GPa pressure was employed and held, then the temperature was increased to 1250–1300 °C, heated there for 8 h, followed by either directly quenching with cold water flowing through the anvil cell or slow cooling to 600 °C then quenching. After the temperature returns to room temperature, the pressure was released. All products were examined by powder X-ray diffraction (XRD). No acentric $BaNiSn_3$-type phase could be detected; rather, mixtures of $CaBe_2Ge_2$-type $SrAu_xSn_{4-x}$, $SrAuSn_2$, tetragonal Sn, and unidentified phase(s) were always produced.

**Differential Scanning Calorimetry (DSC):** Measurements were performed with a Perkin-Elmer differential scanning calorimeter (DSC). Two samples were purposely selected for DSC measurements: (1) 52.2 mg product of nominal $SrAu_{1.75}Sn_{2.25}$ reaction (pure $CaBe_2Ge_2$-type phase) and (2) 28.5 mg product of nominal "$SrAuSn_3$" reaction (a mixture of $SrAuSn_2$ and Sn). Both samples were loaded into Ta tubes (Ø = 3 mm) and laser-sealed in an Ar-filled glovebox. In this way, sample loss due to evaporation at high temperature was avoided during DSC measurements. Each assembly was heated in an argon atmosphere from room temperature to 950 °C at a rate of 20 °K·min$^{-1}$ on heating and cooling.

**X-ray Diffraction:** Phase analyses were accomplished using both powder and single crystal XRD data. Powder data were collected with a STADI P powder diffractometer equipped with Cu-$K_{\alpha1}$ radiation ($\lambda$ = 1.540598 Å). A polycrystalline Si standard (NIST 640b) was added to each sample to calibrate peak positions so that accurate lattice parameters could be compared directly.

Single crystals from $SrAu_ySn_{4-y}$ ($y$ = 1.25, 1.40, 1.75, 2.00, and 2.25) reactions were mounted with a Bruker APEX CCD diffractometer equipped with graphite-monochromatized Mo-$K_\alpha$ ($\lambda$ = 0.71069 Å) radiation. Intensity data were collected at room temperature in mixed $\omega$ and $\phi$ scan modes over $2\theta$ ranging from ca 4° to 60°. Data integration and reduction were completed by the SAINT subprogram included in the SMART software package.[18] Empirical absorption corrections were performed with the aid of the subprogram SADABS. Structure solution and refinements were performed using SHELXTL 6.1.[18] Determination of the space group *P*4/*nmm* was straightforward and direct methods were applied to establish structural models with the help of the XPREP subprogram. All structures were adequately refined; no abnormal phenomena on refinements need to be specially noted.

Table 3 summarizes the crystallographic data and their refinements of the two end members of the $CaBe_2Ge_2$-type $SrAu_xSn_{4-x}$ solid solution, i.e., $SrAu_{1.65(1)}Sn_{2.35(1)}$ and $SrAu_{2.19(1)}Sn_{1.81(1)}$, in addition to $SrAu_2Sn_2$ without any Au/Sn site occupation disorder. Table 4 lists the atomic coordinates and displacement parameters after standardization with the program STRUCTURE TIDY.[25] Displacement parameters of the present $SrAu_2Sn_2$ are about half of that in literature,[15] probably a result of different annealing treatments.

Further details of the crystal structures investigations may be obtained from the Fachinformationszentrum Karlsruhe, 76344 Eggenstein-Leopoldshafen, Germany (Fax: +49-7247-808-666; E-Mail: crysdata@fiz-karlsruhe.de, http://www.fiz-karlsruhe.de/request for deposited data.html) on quoting the depository numbers CSD-428689 ($SrAu_{1.65}Sn_{2.35}$), CSD-428690 ($SrAu_{2.19}Sn_{1.81}$), and CSD-428691 ($SrAu_2Sn_2$).

**Electronic structure calculations:** To understand the coloring of the structural network in $SrAu_xSn_{4-x}$ and the instability of "$SrAuSn_3$",

**Table 3.** Crystallographic data and structural refinements for $SrAu_xSn_{4-x}$, $x$ = 1.65(1), 2, and 2.19(1).

| | $x$ = 1.65 | $x$ = 2 | $x$ = 2.19 |
|---|---|---|---|
| FW /g·mol$^{-1}$ | 691.54 | 718.93 | 733.81 |
| Space group, Z | *P*4/*nmm*, 2 | P4/*nmm*, 2 | *P*4/*nmm*, 2 |
| Lattice parameter | | | |
| $a$ /Å | 4.6528(2) | 4.6651(4) | 4.6233(3) |
| $c$ /Å | 11.3753(4) | 11.277(1) | 11.295(1) |
| $V$ /Å$^3$ | 246.26(2) | 245.43(5) | 241.42(4) |
| $d_{cal}$ /g·cm$^{-3}$ | 9.326 | 9.728 | 10.095 |
| Abs.coeff. /mm$^{-1}$ | 71.294 | 80.201 | 86.318 |
| Refl. coll. /$R_{int}$ | 2698 / 0.0486 | 3360 / 0.0506 | 3385 / 0.0522 |
| Data/restr./ para. | 263 / 0 / 16 | 260 / 0 / 15 | 254 / 0 / 15 |
| GOF | 1.075 | 1.093 | 1.144 |
| $R_1$, $wR_2$ [$I \geq 2\sigma(I)$] | 0.0315 / 0.0829 | 0.0218 / 0.0454 | 0.0308 / 0.0649 |
| $R_1$, $wR_2$ (all data) | 0.0336/0.0842 | 0.0249/0.0462 | 0.0424/0.0680 |
| Ext. coeff. | 0.0046(7) | 0.0038(4) | |
| Residues /e·Å$^{-3}$ | 4.080/–3.161 | 1.677/–1.908 | 1.362/–5.394 |



 

**Table 4.** Atomic coordinates and equivalent isotropic displacement parameters for $SrAu_xSn_{4-x}$, $x$ = 1.65(1), 2, and 2.19(1).

| $x$ | Atom [a)] | Wyck. | Symm. | x | y | z | $U_{eq}$ /Å$^2$ |
|---|---|---|---|---|---|---|---|
| 1.65 | Sr | 2c | 4*mm* | ¼ | ¼ | 0.7545(2) | 0.019(1) |
| | Au1 | 2c | 4*mm* | ¼ | ¼ | 0.3611(1) | 0.019(1) |
| | M2 | 2*a* | –4*m*2 | ¾ | ¼ | 0 | 0.028(1) |
| | Sn3 | 2*b* | –4*m*2 | ¾ | ¼ | ½ | 0.014(1) |
| | Sn4 | 2*c* | 4*mm* | ¼ | ¼ | 0.1277(2) | 0.037(1) |
| 2 | Sr | 2*c* | 4*mm* | ¼ | ¼ | 0.7593(1) | 0.014(1) |
| | Au1 | 2c | 4*mm* | ¼ | ¼ | 0.3624(1) | 0.017(1) |
| | Au2 | 2*a* | –4*m*2 | ¾ | ¼ | 0 | 0.022(1) |
| | Sn3 | 2*b* | –4*m*2 | ¾ | ¼ | ½ | 0.013(1) |
| | Sn4 | 2*c* | 4*mm* | ¼ | ¼ | 0.1268(1) | 0.018(1) |
| 2.19 | Sr | 2*c* | 4*mm* | ¼ | ¼ | 0.7543(2) | 0.014(1) |
| | Au1 | 2c | 4*mm* | ¼ | ¼ | 0.3624(1) | 0.024(1) |
| | Au2 | 2*a* | –4*m*2 | ¾ | ¼ | 0 | 0.024(1) |
| | M3 | 2*b* | –4*m*2 | ¾ | ¼ | ½ | 0.020(1) |
| | Sn4 | 2*c* | 4*mm* | ¼ | ¼ | 0.1275(1) | 0.022(1) |

a) M = 0.66(1) Au + 0.34(1) Sn for $x$ = 1.65 and M = 0.19(1) Au + 0.81(1) Sn for $x$ = 2.19.

electronic structure calculations were performed using the projector augmented wave method (PAW) of Blöchl[26] coded in the Vienna ab initio simulation package (VASP).[27] The generalized gradient approximation (GGA) with exchange and correlation treated by the Perdew-Burke-Enzerhoff (PBE) functions[28] was employed in all VASP calculations. The cutoff energy for the plane wave calculations was set to 500 eV and 84 $k$-points for $SrAu_2Sn_2$, 20 for $AAuSn_3$, and 50 for $AAuSn_2$ ($A$ = Sr, Ba) were used for integrations involving the irreducible wedge of the Brillouin zone. The structures of $SrAuSn_3$ and $SrAuSn_2$ were constructed from the single crystal data of $BaAuSn_3$ and $BaAuSn_2$, respectively. And, all structures, including $AAuSn_3$, $AAuSn_2$ and Sn, used for free energy calculations, were optimized.

For chemical bonding analysis, electronic structure calculations were carried out by the self-consistent, tight-binding linear-muffin-tin-orbital (LMTO)[29] method in the local density (LDA) and atomic sphere (ASA) approximations, within the framework of density functional theory[30] using the Stuttgart code.[31] The ASA radii were scaled automatically, and no interstitial spheres were needed at the criterion of 16 % maximum overlap between neighboring ASA spheres. Reciprocal space integrations were carried out using the tetrahedron method. The basis sets were 5s/(5p)/4d/(4f) for Sr, 6s/(6p)/5d/(5f) for Ba, 6s/6p/5d/(5f) for Au, and 5s/5p/(5d)/(4f) for Sn, with orbitals in parentheses down-folded.[32] Scalar relativistic effects were automatically included in calculations.[33] The Brillouin zone was sampled by 600 $k$-points for $SrAu_2Sn_2$, 301 for $AAuSn_2$ ($A$ = Sr, Ba) and 294 for $AAuSn_3$ in respective irreducible wedges. Crystal orbital Hamilton population (COHP) analyses[34] were performed to assess interatomic orbital interactions.

**Supporting Information** (see footnote on the first page of this article): Further details are given in Tables S1–S5 and Figures S1 and S2.

## Acknowledgements

The research was supported by the Office of the Basic Energy Sciences, Materials Sciences Division, U. S. Department of Energy (DOE). Ames Laboratory is operated for DOE by Iowa State University under contract No. DE-AC02–07CH11358. The theoretical study (by Y.Z.) was supported by National Science Foundation, DMR-12–09135.

## References

[1] a) W. B. Pearson, *J. Solid State Chem.* **1985**, *56*, 278–287; b) E. Parthe, B. Chabot, H. F. Braun, N. Engel, *Acta Crystallogr., Sect. B* **1983**, *39*, 588–595.
[2] Y. Kamihara, T. Watanabe, M. Hirano, H. Hosono, *J. Am. Chem. Soc.* **2008**, *130*, 3296–3297.
[3] a) D. Mandrus, A. S. Sefat, M. A. McGuire, B. C. Sales, *Chem. Mater.* **2010**, *22*, 715–723; b) A. S. Sefat, *Curr. Opin. Solid State Mater. Sci.* **2013**, *17*, 59–64.
[4] E. Bauer, R. T. Khan, H. Michor, E. Royanian, A. Grytsiv, N. Melnychenko-Koblyuk, P. Rogl, D. Reith, R. Podloucky, E. W. Scheidt, W. Wolf, M. Marsman, *Phys. Rev. B* **2009**, *80*, 064504.
[5] V. K. Anand, H. Kim, M. A. Tanatar, R. Prozorov, D. C. Johnston, *Phys. Rev. B* **2013**, *87*, 224510/224511–224510/224522.
[6] N. H. Sung, J.-S. Rhyee, B. K. Cho, *Phys. Rev. B* **2011**, *83*, 094511/094511–094511/094516.
[7] K. Kudo, Y. Nishikubo, M. Nohara, *J. Phys. Soc. Jpn.* **2010**, *79*, 123710/123711–123710/123714.
[8] S. Ganesanpotti, T. Yajima, T. Tohyama, Z. Li, K. Nakano, Y. Nozaki, C. Tassel, Y. Kobayashi, H. Kageyama, *J. Alloys Compd.* **2014**, *583*, 151–154.
[9] Q. Lin, G. J. Miller, J. D. Corbett, *Inorg. Chem.* **2014**, *53*, 5875–5877.
[10] H. R. Khan, *Gold Bull.* **1984**, *17*, 94–100.
[11] M. Isobe, H. Yoshida, K. Kimoto, M. Arai, E. Takayama-Muromachi, *Chem. Mater.* **2014**, *26*, 2155–2165.
[12] a) F. Hulliger, *J. Alloys Compd.* **1995**, *218*, 255–258; b) Y. N. Grin, K. Hiebl, P. Rogl, H. Noel, *J. Less-Common Met.* **1990**, *162*, 371–377; c) Y. N. Grin, P. Rogl, K. Hiebl, *J. Less-Common Met.* **1988**, *136*, 329–338; d) Y. Grin, M. Ellner, K. Hiebl, P. Rogl, O. M. Sichevich, O. M. Myakush, *J. Alloys Compd.* **1994**, *205*, 285–289.
[13] C. Zheng, R. Hoffmann, *J. Am. Chem. Soc.* **1986**, *108*, 3078–3088.
[14] A. V. Tkachuk, A. Mar, *J. Solid State Chem.* **2007**, *180*, 2298–2304.
[15] C. Schwickert, B. Gerke, R. Pöttgen, *Z. Naturforsch. B* **2014**, *69*, 767–774.
[16] S. Esmaeilzadeh, R. D. Hoffmann, R. Pöttgen, *Z. Naturforsch. B* **2004**, *59*, 1451–1457.
[17] R.-D. Hoffmann, R. Pöttgen, D. Kußmann, D. Niepmann, H. Trill, B. D. Mosel, *Solid State Sci.* **2002**, *4*, 481–487.
[18] *SHELXTL*, 6.10 ed., Bruker Analytical X-ray Systems, Inc., Madison, WI. **2000**.
[19] G. J. Miller, *Eur. J. Inorg. Chem.* **1998**, 523–536.



 

[20] P. Villars, L. D. Calvert, *Pearson's Handbook of Crystallographic Data for Intermetallic Phases*, vol. 1, 2nd ed., American Society of Metals, Materials Park, OH, **1991**.
[21] Q. Lin, J. Vetter, J. D. Corbett, *Inorg. Chem.* **2013**, *52*, 6603–6609.
[22] Q. Lin, unpublished results.
[23] J. K. Burdett, G. J. Miller, *Chem. Mater.* **1990**, *2*, 12–26.
[24] a) S. K. Kim, M. E. Tillman, H. Kim, A. Kracher, S. L. Bud'ko, R. Prozorov, P. C. Canfield, *Superconductor Sci. Technol.* **2010**, *23*, 054008; b) T. Kondo, A. F. Santander-Syro, O. Copie, C. Liu, M. E. Tillman, E. D. Mun, J. Schmalian, S. L. Bud'ko, M. A. Tanatar, P. C. Canfield, A. Kaminski, *Phys. Rev. Lett.* **2008**, *101*, 147003.
[25] L. M. Gelato, E. Parthé, *J. Appl. Crystallogr.* **1987**, *20*, 139–143.
[26] a) P. E. Blöchl, *Phys. Rev. B* **1994**, *50*, 17953–17979; b) G. Kresse, D. Joubert, *Phys. Rev. B* **1999**, *59*, 1758–1775.
[27] a) G. Kresse, J. Furthmüller, *Comput. Mater. Sci.* **1996**, *6*, 15–50; b) G. Kresse, J. Furthmüller, *Phys. Rev. B* **1996**, *54*, 11169–11186.
[28] J. P. Perdew, K. Burke, M. Ernzerhof, *Phys. Rev. Lett.* **1996**, *77*, 3865–3868.
[29] a) H. L. Shriver, *The LMTO Method*, Springer-Verlag, Berlin, Germany, **1984**; b) K. Anderson, O. O. Jepsen, *Phys. Rev. Lett.* **1984**, *53*, 2571; c) O. K. Andersen, O. Jepsen, M. Snob, *Linearized Band Structure Methods*, in *Lecture Notes in Physics: Electronic Band Structure and Its Applications* (Ed.: M. Yussou), Springer Verlag, Berlin, Germany, **1987**.
[30] R. Tank, O. Jepsen, A. Burckhardt, O. K. Andersen, Max-Planck-Institut für Festkörperforschung, Stuttgart, Germany, **1988**.
[31] R. Tank, O. Jepsen, A. Burkhardt, O. K. Andersen, TB-LMTO-ASA Program, Vers. 4.7, Max-Planck-Institut für Festkörperforschung, Stuttgart, Germany, **1994**.
[32] W. R. L. Lambrecht, O. K. Andersen, *Phys. Rev. B* **1986**, *34*, 2439.
[33] D. D. Koelling, B. N. Harmon, *J. Phys. C Solid State Phys.* **1977**, *10*, 3107–3114.
[34] R. Dronskowski, P. E. Bloechl, *J. Phys. Chem.* **1993**, *97*, 8617–8624.

Received: November 21, 2014
Published Online: December 22, 2015



 